J. Fluid Mech. (2008), *vol.* 608, *pp.* 21–41. © 2008 Cambridge University Press
doi:10.1017/S0022112008001183 Printed in the United Kingdom

Microbubbly drag reduction in Taylor–Couette flow in the wavy vortex regime

KAZUYASU SUGIYAMA†, ENRICO CALZAVARINI‡
AND DETLEF LOHSE

Physics of Fluids Group, Department of Applied Physics, J. M. Burgers Centre for Fluid
Dynamics, and Impact-, MESA-, and BMTI-Institutes, University of Twente, P.O. Box 217,
7500 AE Enschede, The Netherlands
d.lohse@utwente.nl

(Received 8 March 2007 and in revised form 24 February 2008)

We investigate the effect of microbubbles on Taylor–Couette flow by means of direct numerical simulations. We employ an Eulerian–Lagrangian approach with a gas–fluid coupling based on the point-force approximation. Added mass, drag, lift and gravity are taken into account in the modelling of the motion of the individual bubble. We find that very dilute suspensions of small non-deformable bubbles (volume void fraction below 1 %, zero Weber number and bubble Reynolds number $\lesssim 10$) induce a robust statistically steady drag reduction (up to 20 %) in the wavy vortex flow regime ($Re = 600$–2500). The Reynolds number dependence of the normalized torque (the so-called torque reduction ratio (TRR) which corresponds to the drag reduction) is consistent with a recent series of experimental measurements performed by Murai *et al.* (*J. Phys. Conf. Ser.* vol. 14, 2005, p. 143). Our analysis suggests that the physical mechanism for the torque reduction in this regime is due to the local axial forcing, induced by rising bubbles, that is able to break the highly dissipative Taylor wavy vortices in the system. We finally show that the lift force acting on the bubble is crucial in this process. When it is neglected, the bubbles preferentially accumulate near the inner cylinder and the bulk flow is less efficiently modified. Movies are available with the online version of the paper.

1. Introduction

Drag reduction induced by injection of a small concentration of gas bubbles in a liquid flow has been addressed in several physical systems, from a turbulent boundary layer on a flat plate (Madavan, Deutsch & Merkle 1984; Ferrante & Elghobashi 2004; Sanders *et al.* 2006), to channel flows (Xu, Maxey & Karniadakis 2002; Lu, Fernández & Tryggvason 2005). Despite the effort devoted to the subject, the problem has not been fully clarified from a fundamental physical point of view. Different mechanisms such as effective compressibility of the flow (Ferrante & Elghobashi 2004), and bubble deformability (Lu *et al.* 2005) or compressibility (Lo, L'vov & Procaccia 2006) or splitting (Meng & Uhlman 1998), have been proposed as relevant. A misleading aspect of the drag-reduction problem arises from the fact that, depending on the system considered, either transient or spatially dependent (as a function of the

---

†Present address: sugiyama@fel.t.u-tokyo.ac.jp
‡Present address: enrico.calzavarini@ens-lyon.fr

bubbles injection point) or statistically steady effects can be observed. To overcome this difficulty, more recently experiments have been conducted in a Taylor–Couette (TC) setup (Djeridi, Gabillet & Billard 2004; van den Berg *et al.* 2005; Murai, Oiwa & Takeda 2005; van den Berg *et al.* 2007). The TC system has two advantages. First, since it is a closed system, an exact global energy balance relation can be explicitly obtained and drag variations can be evaluated in terms of a single globally averaged quantity, the torque. Second, statistically stationary states can be reached easily. In order to quantify the level of drag reduction, it is convenient to consider the so called torque reduction ratio (TRR) coefficient,

$$\mathrm{TRR} \equiv 1 - \frac{T_b}{T}, \tag{1.1}$$

where T_b stands for the measured torque in the two-phase system, i.e. with the bubbles included, and T for the torque in the single-phase flow at the same Reynolds number. In the highly turbulent TC system ($Re > 10^5$) drag reduction is mainly attributed to the bubble deformation mechanism (van den Berg *et al.* 2005; Lu *et al.* 2005) in the boundary layer (van den Berg *et al.* 2007).

Also, at moderate flow Reynolds numbers in the range $Re = 600$–4500 (the so-called wavy/modulate-wavy Taylor vortex regime) Murai *et al.* (2005) reported that bubble-induced drag reduction up to 25 % can be observed for tiny bubble concentrations, $O(0.1\,\%)$ in volume. The experimental apparatus considered by these authors is forced by rotation of the inner cylinder, while the outer one is kept fixed. The cylindrical enclosure is filled with a silicon oil roughly five times more viscous than water ($\nu = 5 \times 10^{-6}\,\mathrm{m^2\,s^{-1}}$) and air bubbles are injected into the fluid. Their typical radius is $a = 250$–$300\,\mu\mathrm{m}$ and Weber number $We \equiv 2a\rho v_T^2 \sigma^{-1} < 0.6$ (where ρ and σ are respectively the density and the surface tension of the oil and v_T the bubble terminal velocity in still fluid). The bubble Reynolds number, based on v_T, is $Re_b = 2a\ v_T/\nu \simeq 7$. Therefore bubbles can be regarded with a good approximation as mono-disperse non-deformable spheres, whose scale is of the same order as the smallest scales of fluid fluctuations. The experimental results of Murai *et al.* showed that the drag reduction decreases with increasing Reynolds number. TRR was almost vanishing at $Re \simeq 4000$ and became negative (drag increase) for even larger Reynolds numbers. Murai *et al.* explained this drag reduction effect through the bubble interaction with the coherent Taylor vortices, producing a vertical elongation of their arrangement.

The features of the Murai *et al.* experiment, in particular the low large-scale Re and the small (i.e. limited Re_b) non-deformable bubbles employed there, make this experiment accessible to a comparison with numerical simulations, which we will perform in this paper.

The aim is to shed more light on the physical mechanism of drag reduction observed in the flow conditions of Murai *et al.*'s experiment. However, given the complexity of this two-phase flow system, appropriate modelling of the dynamics is unavoidable and approximations must be introduced. First, we use an Eulerian–Lagrangian algorithm. The forces on each point bubble are modelled through effective drag and lift forces; they act back on the fluid through two-way coupling. Second, in order to make the simulation computationally feasible, we have to restrict the flow to a smaller domain than in the experiment and to adopt different, i.e. periodic, boundary conditions. Third, in order to achieve good convergence, the bubbles are initially positioned randomly throughout the flow. This is obviously different from the experimental procedure. In the experiment bubbles are injected from the bottom. The injection sites are close to the inner cylinder walls. The bubbles emerge at the free surface at

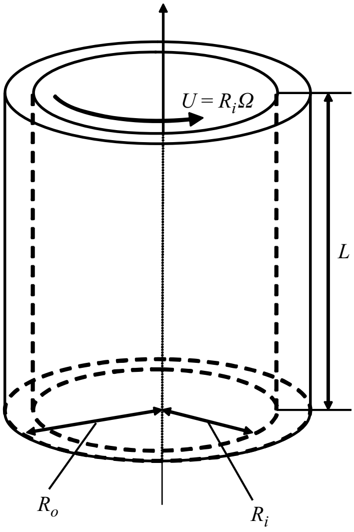

FIGURE 1. Sketch of the Taylor–Couette system.

the top after travelling across the cylindrical enclosure, whose aspect ratio is much larger than in the simulation (cf. the Γ values in table 1 below). It is at the top TC section that the radial mean void fraction is finally measured. The experimenters assumed that the bubble distribution rapidly reaches a fully developed state that is independent of the inhomogeneous injection sites. This assumption justifies the different bubble injection procedure adopted in our numerics.

In spite of these unavoidable differences, we think – and we will further demonstrate in the paper – that the main flow features and the resulting drag reduction phenomena are reasonably well captured by our numerical approach. In particular, it is of relevance to note that the drag reduction mechanism observed in the flow conditions examined here – which we will call *pseudo-turbulent* drag reduction – turns out to be substantially different from the mechanism that acts under the highly turbulent conditions explored by van den Berg *et al.* (2005, 2007). Under those conditions the bubble deformation turned out to be crucial, see also Lu *et al.* (2005).

The paper is organized as follows: in § 2, we introduce the geometry and the two-phase model system used for the numerical study and present a test in order to validate the code. In § 3 our numerical results on torque modulation in the two-phase flow and bubble distributions are described and discussed in detail. Section 4 contains comments and conclusions. In the Appendix we derive relations connecting globally averaged quantities in the TC system.

2. Taylor–Couette system and numerical scheme

2.1. *Definitions*

In the Taylor–Couette system the fluid is enclosed between two coaxially rotating cylinders with radius R_o and R_i, respectively; for the outer and the inner ones. The height of the cylindrical enclosures, denoted L, is in the vertical direction. We limit our investigation to the case where only the inner cylinder is rotating at a constant angular velocity Ω while the outer one is at rest, see figure 1. Furthermore, no-slip conditions are assumed at the walls. It is convenient to adopt the Reynolds number based on the inner cylinder velocity $U = R_i\Omega$ and the gap width $d = (R_o - R_i)$ as a control parameter, that is

$$Re \equiv \frac{(R_o - R_i)R_i\Omega}{\nu}. \tag{2.1}$$

The response of the system is the time-averaged torque on the inner cylinder, which is expressed as

$$T = 2\pi R_i^2 L\tau_{wi}, \tag{2.2}$$

where τ_{wi} stands for the mean inner-wall shear stress. In cylindrical coordinates (z, r, θ) the wall shear stress can be computed as

$$\tau_{wi} = -\rho\nu\left(\frac{\mathrm{d}}{\mathrm{d}r}\overline{u_\theta}|_{r=R_i} - \Omega\right), \tag{2.3}$$

where u_θ is the azimuthal velocity component and the overbar denotes averaging in space over concentric cylindrical surfaces and time. Note that an analogous expression for the torque can be written in terms of the outer cylinder, since conservation of angular momentum implies

$$\left(\frac{\mathrm{d}}{\mathrm{d}r}\overline{u_\theta}|_{r=R_o}\right)R_o^2 = \left(\frac{\mathrm{d}}{\mathrm{d}r}\overline{u_\theta}|_{r=R_i} - \Omega\right)R_i^2.$$

On increasing angular velocity the flow between the two cylinders experiences several hydrodynamic instabilities. After the destabilization of the laminar flow, the formation of horizontal couples of circular rolls, known as Taylor vortices (Taylor 1923), is observed. Then, on further increasing Ω, axial symmetry is lost and first steady wavy, then time-modulated rolls appear, and finally a fully developed turbulent regime is established, see Andereck, Liu & Swinney (1986).

The relation linking the torque to the Reynolds number and the gap parameter $\eta = R_i/R_o$ cannot be directly computed from the equation of motion, except for the laminar (Couette) regime. Deduction under general conditions of the functional relation $T(Re, \eta)$ is still an open problem, see Lathrop, Fineberg & Swinney (1992), Esser & Grossmann (1996), Eckhardt, Grossmann & Lohse (2000, 2007) and Lim & Tan (2004). However, the torque can be related to the mean (time- and volume-averaged $\langle \ldots \rangle$) energy dissipation rate $\langle \varepsilon \rangle$, namely[†]

$$\langle \varepsilon \rangle = \frac{T\Omega}{\pi\rho\left(R_o^2 - R_i^2\right)L}. \tag{2.4}$$

Thus $\langle \varepsilon \rangle$ and T are directly proportional and a decrease in the torque corresponds to a reduction of the internal energy dissipation rate in the system. Therefore, the total drag reduction can be deduced from the variations of a single global observable such as the torque.

2.2. *The model for the two-phase flow*

The direct numerical simulation (DNS) approach we adopt is based on the Eulerian–Lagrangian algorithm, in the form used by Mazzitelli, Lohse & Toschi (2003*a*, *b*). The fluid phase is described by the Navier–Stokes equation for an incompressible flow ($\nabla \cdot \boldsymbol{u} = 0$). Bubbles act on the flow through a two-way point-like coupling:

$$\partial_t \boldsymbol{u} + (\boldsymbol{u}\cdot\nabla)\,\boldsymbol{u} = -\frac{\nabla p}{\rho} + \nu\ \nabla^2\boldsymbol{u} + \boldsymbol{f}_b, \tag{2.5}$$

[†] Note that in Lathrop *et al.* (1992) and in van den Berg *et al.* (2005) this relation contains a typographical error, namely, a wrong pre-factor 2. See also the Appendix.

$$\boldsymbol{f}_b = \sum_{i}^{N_b} \frac{4\pi a^3}{3} \delta\big(\boldsymbol{x} - \boldsymbol{y}_{(i)}\big) \left(\partial_t \boldsymbol{u} + (\boldsymbol{u}\cdot\nabla)\boldsymbol{u} - \boldsymbol{g}\right), \tag{2.6}$$

where $\boldsymbol{y}_{(i)}$ denotes the instantaneous position of the ith bubble and $\boldsymbol{g}$ the gravitational acceleration. The bubbles are tracked as Lagrangian particles with a model equation in which added mass, drag, lift, and gravity are taken into account. Their dynamics is given by Maxey & Riley (1983), Auton (1987), Auton, Hunt & Prud'homme (1988), Climent & Magnaudet (1999), Mazzitelli *et al.* (2003*b*):

$$\frac{\mathrm{d}\boldsymbol{y}}{\mathrm{d}t} = \boldsymbol{v}, \tag{2.7}$$

$$\frac{\mathrm{d}\boldsymbol{v}}{\mathrm{d}t} = 3\left(\partial_t \boldsymbol{u} + (\boldsymbol{u}\cdot\nabla)\,\boldsymbol{u}\right) - \frac{1}{\tau_b}(\boldsymbol{v}-\boldsymbol{u}) - 2\boldsymbol{g} - (\boldsymbol{v}-\boldsymbol{u})\times\boldsymbol{\omega}, \tag{2.8}$$

with $\tau_b \equiv a^2/(6\nu)$ the characteristic bubble response time, and $\boldsymbol{u}$ and $\boldsymbol{\omega}$ denoting respectively the fluid velocity and vorticity vectors at the bubble position. Fully elastic boundary conditions are assumed for the bubbles on the cylinder's lateral walls, while direct bubble–bubble interactions (four-way coupling) are neglected. It is important to note that the lift force in (2.8) is only approximate. Here the expression for the rotational flow in the limit $Re_b \rightarrow \infty$ is used, corresponding to a lift coefficient $C_L = 1/2$ (Auton 1987). However, in the simulation we consider the case of $Re_b \sim O(10)$ in an unsteady flow for which the Auton's expression may be incorrect or may overestimate the intensity of the lift force (van Nierop *et al.* 2007). Despite these approximations and the simplified approach of the model adopted, it has been shown by van den Berg, Luther & Lohse (2006) and Calzavarini *et al.* (2008), that qualitative agreement with real systems occurs. We will further discuss the effect of lift on the bubble dispersion in TC flow in § 3.5.

2.3. *Numerical implementation, code validation and tuning of the DNS*

The continuous phase, (2.5), has been implemented in cylindrical coordinates on a finite-difference scheme. The grid, $N_z \times N_r \times N_\theta = 128 \times 64 \times 256$, is non-uniform and refined in the near-wall regions in the radial direction, while it is uniform both in the vertical and azimuthal ones. Careful attention has been paid to the implementation of the nonlinear term by the use of an algorithm that has highly conservative properties for energy, proposed by Fukagata & Kasagi (2002). The time marching scheme is of second-order accuracy. The bubble trajectories (2.7)–(2.8) have also been implemented in cylindrical coordinates as in Djeridi *et al.* (2004) and integrated by a second order scheme in time, while interpolation of fluid velocity at the bubble position is implemented by a third-order scheme, i.e. taking into account up to the second nearest lattice nodes (64 points). The feedback (2.6) is extrapolated from the bubble position to the next nearest nodes by a tri-linear scheme (8 points). We use periodic boundary conditions in the vertical direction both for the fluid and the bubbles. Additionally, for the fluid only, we fix the mean flow in the vertical direction to be zero, in order to avoid the emerging of a mean axial current that would prevent a realistic comparison with the experiment, where it is forbidden for geometrical reasons.

The implementation of the single-phase flow dynamics has been validated by measuring the onset of the primary instability, i.e. the critical Reynolds number as a function of the gap ratio, $Re_c(\eta)$, as well as the dimensionless torque $G = T/(\rho\nu^2 L)$ at different Reynolds numbers and for different values of (the gap ratio) η. The results for $Re_c(\eta)$ were compared with the available analytical calculations, Taylor (1923)

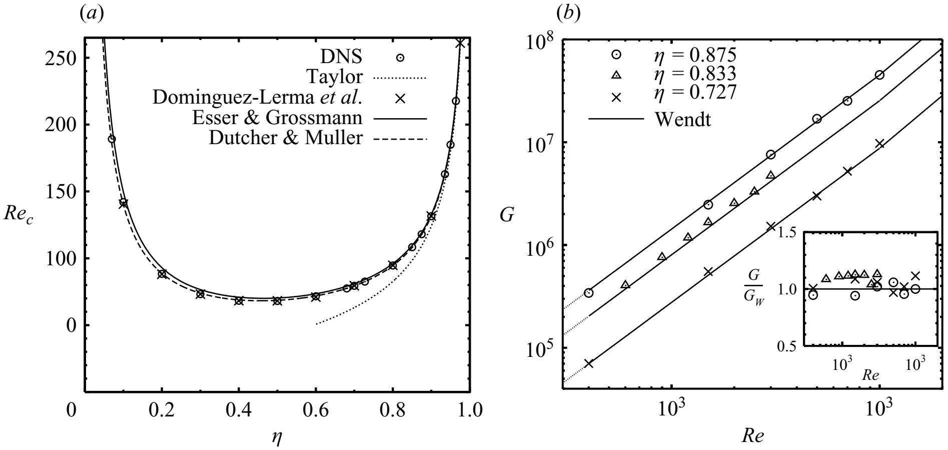

FIGURE 2. Single-phase flow code validation. (*a*) The critical Reynolds number Re_c as a function of the gap ratio η, and comparison with Taylor (1923) narrow-gap limit ($\eta \rightarrow 1$), Dominguez-Lerma *et al.* (1984), Esser & Grossmann (1996) and Dutcher & Muller (2007) predictions. (*b*) Dimensionless torque $G = T/(\rho \nu^2 L)$ versus Re for three different values of the gap ratio η, and comparison with Wendt's empirical relation $G_W = 1.45(Re\ \eta)^{3/2}/(1-\eta)^{7/4}$, Wendt (1933). The inset shows a compensated plot G/G_W vs. Re.

(for the narrow-gap limit $\eta \rightarrow 1$), Dominguez-Lerma, Ahlers & Cannell (1984) and with phenomenological estimates given by Esser & Grossmann (1996) and Dutcher & Muller (2007). Moreover we compare $G(\eta, Re)$ with the empirical law given by Wendt (1933) (also in Lathrop *et al.* 1992), finding satisfactory agreement (figure 2).

The tuning of our DNS to the experimental setup adopted by Murai *et al.* is then done as follows. The experimental apparatus is geometrically characterized by a gap ratio $\eta = 5/6$ and an aspect ratio $\Gamma = L/d = 20$, see figure 1 of Murai *et al.* (2005) for a sketch of their setup. The flow boundaries in the experiment on the horizontal surfaces are free fluid surface (free slip) at the top and zero mass flux at the bottom. Since we do not expect drag to be strongly affected by the influence of the top/bottom boundary conditions, particularly for aspect ratio values (Γ) much larger than one, we use, for simplicity and in order to limit the computational costs, a smaller aspect ratio $L/d = 8$ than in the experiment, and periodic boundary conditions as mentioned before. The gap ratio is as in the experiment, $\eta = 5/6$. It turned out that the constraint of periodic boundaries to the flow may introduce a bias in the formation and breaking of coherent structures in the flow; we will comment on this point in detail in § 3.2. Furthermore, for the whole set of numerical simulations we fix the ratio a/d and the bubble Reynolds number Re_b to the experimental values – neither of these quantities are Reynolds dependent in the experiment – and we vary the fluid Reynolds number Re, by changing the inner cylinder rotational speed Ω as in the experimental setup, in the range $Re = 600$–2500. Care has to be taken when tuning of the void fraction, since in the experiment it was not kept constant among the different runs but estimated *a posteriori* through measuring the total gas flow rate. We chose the total void fraction α_0 to be consistent with the experiment. The values (table 1 below) are obtained by a fit to the estimated experimental void fraction (see also Oiwa 2005, chap. 5); this explains some tiny deviations between the two cases. For the flow conditions that we consider for the comparison, i.e. $Re \leqslant 2500$, α_0 is always less than 1 %. The values of the ratio a/d and the total void fraction value α_0 then fix the number of bubbles

	η	Γ	a/d	b.c.	Re	α_0 (%)	Re_b	We
Exp.	5/6	20	1/40	vert. no-slip, horiz. top free-slip, horiz. bottom zero-mass flux	600–4500	0.092 at $Re = 600$ 0.721 at $Re = 2700$ 2.446 at $Re = 4200$	7.1	$\leqslant 0.6$
Sim.	5/6	8	1/40	vert. no-slip, horiz. periodic	600–2500	0.125 at $Re = 600$ 0.670 at $Re = 2500$	7.1	0

TABLE 1. Relevant scales and parameters for the two-phase Taylor–Couette system studied experimentally by Murai *et al.* (2005) and numerically in this paper. We list first the three geometrical parameters: gap ratio η, aspect ratio Γ, and the ratio between the bubble radius and the gap width a/d, then the flow boundary condition, and the large-scale flow Reynolds number range. Finally, bubble characteristics are listed: the global volume void fraction α_0 (in per cent), and the bubble's typical Reynolds and Weber numbers.

we must use in the numerical study, namely $N_b = \alpha_0(\pi L(R_o^2 - R_i^2))/\frac{4}{3}\pi a^3$. The number of bubbles N_b varies between few thousand and a maximum of roughly 1.5×10^4. Table 1 summarizes the set of parameters adopted for the simulations and the experiment.

A typical simulation run at a given value of the Reynolds number is composed of two parts. First, a single-phase DNS is performed until statistical stationarity is reached. Then bubbles are positioned in the flow with a random homogeneous distribution and velocities equal to the local fluid velocity. This bubble injection procedure is supposed to mimic the presumably fully developed state at the top TC section where the bubble distributions have been measured in the experiment. Simultaneously with the bubble injection, the bubbles–fluid (two-way) coupling is activated. The two-phase simulation is then performed until a statistically steady state is well established. All relevant physical observables in the single- and two-phase flow are computed by suitable time averages, of $O(10^2)$ revolution times $(=2\pi\Omega_i^{-1})$, in the statistically stationary regime.

Finally, in order to verify the consistency of the model used in the DNS, we check whether the smallest scale in the system is of the same order as the bubble typical size. In particular we compare the bubble radius a with the size of the Kolmogorov dissipative scale $\eta = (\nu^3/\langle\varepsilon\rangle)^{1/4}$ and, in addition, we look at the magnitude of the wall-units radial size $a^+ \equiv a\sqrt{\tau_w/(\rho\nu^2)}$. While the ratio a/η is relevant in the bulk flow a^+ is of importance in near-wall regions. The results reported in figure 3 show that our assumption of point bubbles is reasonable.

3. Numerical results

3.1. *Overview*

In this section we present the comparison of numerical and experimental results. In figure 4 we show both TRR obtained from the experiment and from the simulations. In the inset TRR is normalized by the total void fraction (this ratio is called the sensitivity by Murai *et al.* 2005). The quantitative agreement on this observable is satisfactory. First, we detect a robust (up to 20 %) statistically steady drag reduction. Second, the drag reduction effect has a decreasing trend for increasing the Reynolds number. How can these two observations be explained? Sections 3.2 and 3.4 are devoted to understanding the physical mechanism leading to this behaviour.

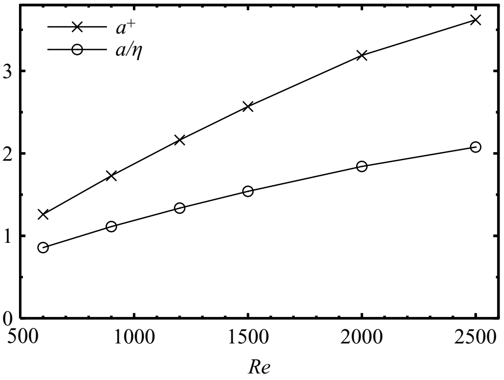

FIGURE 3. Ratio a/η between bubble radius and Kolmogorov scale (circles) and ratio $a^+ = a\sqrt{\tau_w/(\rho\nu^2)}$ between bubble radius and wall length unit (+), both as a function of *Re*. Both the Kolmogorov length η and the wall shear stress τ_w are evaluated on the single-phase flows. The thickness of the viscous-sublayer (l_v) in a planar channel flow in wall units is roughly $l_v^+ \simeq 5$.

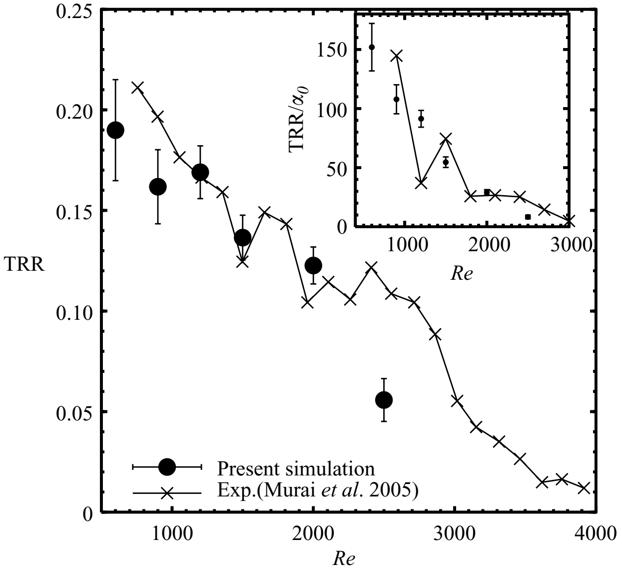

FIGURE 4. Torque reduction ratio computed in the numerical simulations and the experimental measurements performed by Murai *et al.* (2005). In the inset TRR is divided by the mean void fraction α_0. Note that the void fraction is not kept constant with *Re*, see table 1.

Less satisfactory is the comparison with the experiment of the local mean void fraction (or mean bubble concentration). In figure 5 we show the mean radial bubble concentration profiles normalized by the total void fraction, both from the numerical simulations and from the experiment. This quantity is defined as

$$\frac{\overline{\alpha}(r)}{\alpha_0} = \frac{R_o^2 - R_i^2}{2N_b} \frac{1}{T_s} \int_{t_0}^{t_0+T_s} \mathrm{d}t \sum_{i}^{N_b} \frac{\delta(r - y_{r(i)}(t))}{r}, \tag{3.1}$$

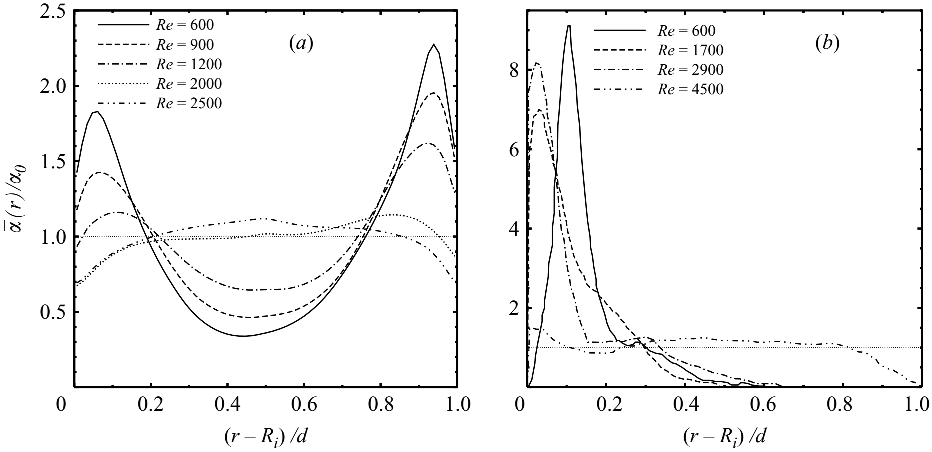

FIGURE 5. Normalized mean local void fraction in the radial direction, $\overline{\alpha}(r)/\alpha_0$, at different Re values, in the numerics (*a*) and the experiment (*b*). The quantity $\overline{\alpha}(r)/\alpha_0$ has been adopted from the data in figure 9 of Murai *et al.* (2005). For better comparison the homogeneous distribution line $\overline{\alpha}(r)/\alpha_0 = 1$ is also shown.

where $y_{r(i)}(t)$ is the radial component of the position vector of the ith bubble and T_s indicates the time interval where the two-phase flow is in statistically steady conditions. The local bubble concentration in the simulations is less inhomogeneous than in the experiment. The maximum deviation from equi-distribution is about 100 % of the homogeneous case and is peaked both at the inner and the outer walls. On the other hand, in the experiment, where radial mean void fraction has been evaluated by averaging over a series of snapshots taken in the upper part of the TC system, a much stronger accumulation peaked near the inner cylinder is found and it reaches much larger values (roughly 4 times larger than the numerics in the most extreme case $Re = 600$). Nevertheless, the same trend towards homogenization at increasing Reynolds number is observed in both cases. The possible origin of this discrepancy and its relevance to drag reduction will be further discussed in detail and will be the focus of § 3.5.

3.2. *Origin of the drag reduction*

The variation of the intensity of the torque in the TC system is directly connected to a change in the mean azimuthal velocity profile along the radial direction $\overline{u_\theta}(r)$, see (2.2)–(2.3). Figure 6(*a*) shows the modification of the two-phase profile compared to the single-phase at two different Reynolds numbers, $Re = 900$ and $Re = 2000$. These Re values will be adopted as reference cases in the following discussion. A smoother slope is observed in figure 6 for the gradient of $\overline{u_\theta}(r)$ at the wall in the two-phase case. As consequence the torque is reduced. We also note that the torque T_b for the two-phase system, when normalized by the torque $T_l = \rho \Omega^2 R_i^4 L/(\eta(1+\eta)Re)$ in the (single-phase) laminar regime, satisfies the following relation (derived in the Appendix):

$$\frac{T_b}{T_l} = 1 + Re\,\frac{\eta}{1-\eta}\,\frac{1}{(\Omega R_i)^2}\int_{R_i}^{R_o} \mathrm{d}r \left(\frac{\overline{u_r u_\theta}(r)}{r} + \left(\frac{r^2}{R_o^2} - 1\right)\frac{\overline{f_{b,\theta}}(r)}{2}\right), \tag{3.2}$$

where $\overline{u_r u_\theta}(r)$ is the azimuthal–radial component of the mean Reynolds shear stress and $\overline{f_{b,\theta}}(r)$ the mean azimuthal component of bubble forcing. Relation (3.2) reveals

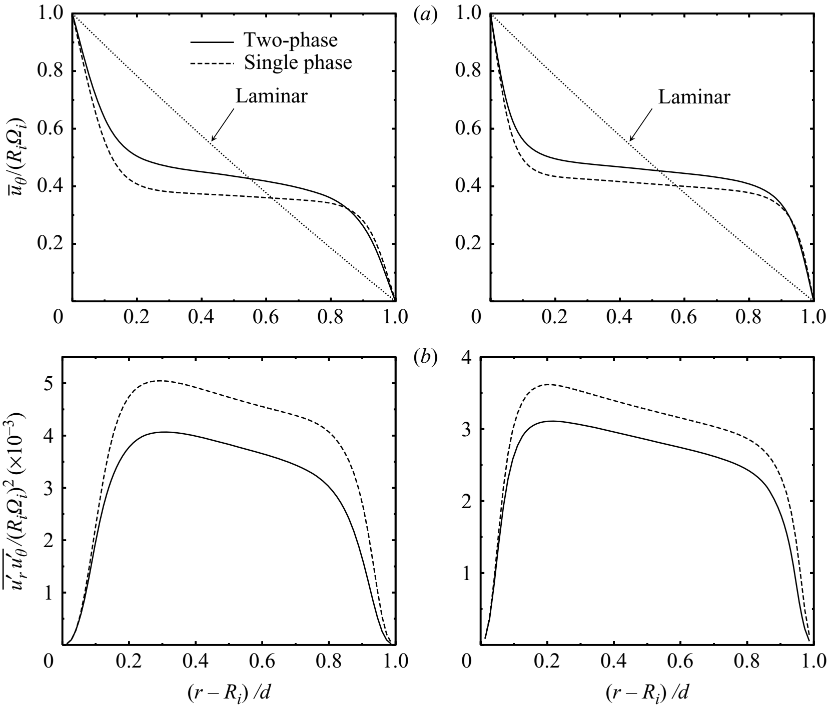

FIGURE 6. (*a*) Mean azimuthal velocity profile $\overline{u_\theta}(r)$ at $Re=900$ (left) and $Re=2000$ (right). The laminar profile is also reported. (*b*) The mean Reynolds shear stress component $\overline{u_\theta u_r}(r)$ at $Re=900$ (left) and $Re=2000$ (right).

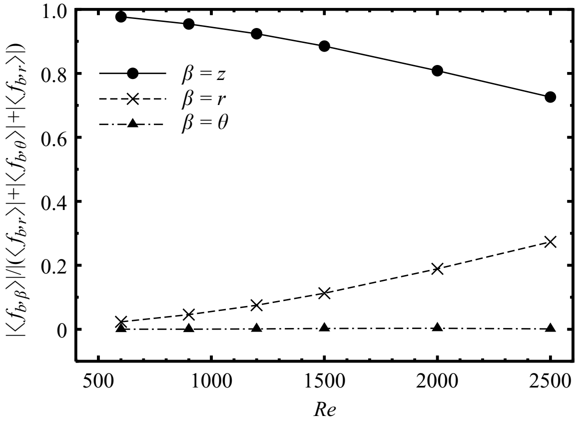

FIGURE 7. Normalized globally averaged (space and time) relative components of the bubble forcing $|\langle f_{b,\beta}\rangle|/(|\langle f_{b,\theta}\rangle| + |\langle f_{b,r}\rangle| + |\langle f_{b,z}\rangle|)$ with $\beta = z, r, \theta$ vs. Re.

the connection between the Reynolds shear stress, the bubble forcing, and the torque. We have checked that in the two-phase case the mean bubble forcing $\boldsymbol{f}_b$ is mainly dominated by the vertical component, see figure 7. Therefore in relation (3.2) the contribution from $\overline{f_{b,\theta}}(r)$ is negligible compared to the Reynolds shear stress and measuring $\overline{u_r u_\theta}(r)$ is a direct way to appreciate the variations in the mean flow

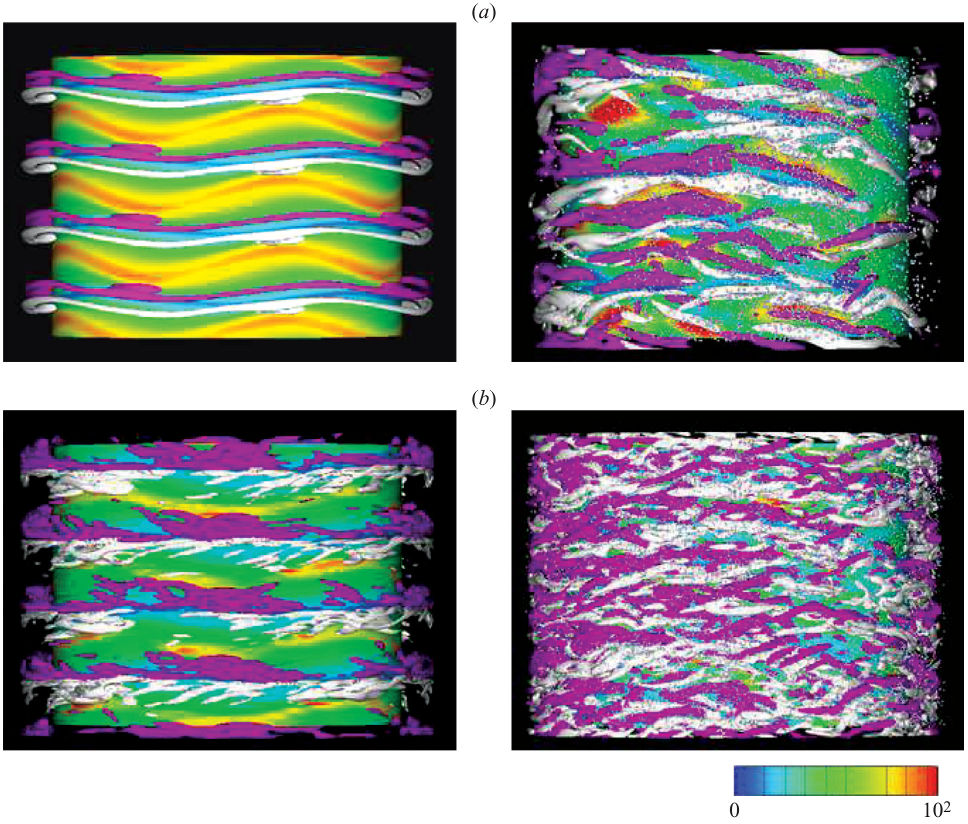

Figure 8. Flow visualization at $Re = 900$ (*a*) and $Re = 2000$ (*b*): Single-phase flow (left) and two-phase flow (right). The Taylor vortex structures are identified by iso-surfaces defined by the relation $(\partial_i u_j)(\partial_j u_i) = -0.4$, and coloured (white and violet) accordingly to the sign of ω_θ on the surfaces. The wall shear stress, measured in $\rho(R_i \Omega)^2$ units, is reproduced in colour on the inner cylinder surface. (Corresponding movies are available with the online version of the paper.)

features responsible for a torque change. As shown in figure 6(*b*), this variation appears to be relevant in the whole bulk of the system and is approximately constant through it, both at large and small Reynolds numbers.

We also have previously observed that in the relative low-Reynolds-number range under consideration, coherent flow structures in the form of Taylor vortices are persistent in the flow. To reveal the effect of the interaction of the dispersed bubbly phase with the coherent flow structures, we present a visualization of the flow. Figure 8 shows snapshots from two simulations respectively at $Re = 900$ and $Re = 2000$, both in the single-phase and in two-phase case. Vortical structures are identified by iso-surfaces of the second invariant of the velocity gradient tensor and are shown in colour accordingly to the sign of the azimuthal component of the local vorticity field, ω_θ (Hunt, Wray & Moin 1988; Tanahashi, Iwase & Miyauchi 2001). The intensity of the inner-shear stress, τ_{wi}, is also reproduced in colour in the figure. Vortical Taylor structures, which come in counter-rotating pairs, are well captured by this visualization method. In both cases it is evident how the addiction of microbubbles efficiently breaks the self-organized order established by the system in the single-phase condition.

3.3. *Effect of bubbles on Taylor vortices*

We now have a more detailed look at the Taylor vortices and how they are affected by the bubble injection. We note that in a periodic TC flow Taylor vortex rolls appear only in even numbers. A Fourier spectral analysis of the azimuthal vorticity component on the mid-cylindrical surface of the gap, $\omega_\theta(r=R_i+d/2, z)$, reveals that the numerically simulated single-phase TC flow displays respectively eight Taylor vortices for Reynolds numbers $Re \leqslant 2000$ and six above this threshold ($Re > 2000$). The two-phase flow on the other hand shows a different behaviour at small Reynolds number, in particular for $Re \leqslant 900$ we observe only six Taylor vortices, while the same number of rolls as the single-phase case is realized for $Re > 900$. This is qualitatively consistent with the experiments by Murai *et al.* (2005), as they observe an elongation of Taylor vortex spacing (i.e. the centre-to-centre distance) in the two-phase case compared to the single-phase case. Such elongation decreases as Re is increased. The single-phase/two-phase elongation ratio in the low-Reynolds-number regime $Re \leqslant 900$ is roughly 30 % both in the simulations and in the experiment. However, we cannot rule out that the even-parity constraint imposed by the periodic boundary condition in the DNS may introduce some kind of artifact in the overall stability of Taylor vortex couples. Also, we note that the experimental measurements, see Murai *et al.* (2005) figure 13, were performed with larger bubbles ($a = 1$ mm), compared to the TRR measurements discussed in that paper ($a = 0.3$ mm). The bubbles employed to quantify the vortex elongation in the experiment turn out to correspond roughly to $Re_b = 400$ and $We = 90$ and they are normally in a *wobbling* state (Grace 1973). Such conditions lie outside the range of applicability of the Eulerian–Lagrangian model and they prevent us attempting a comparison with the DNS.

We now focus on the azimuthal wavelength dependence in the DNS flow. We note that any signature of a dominant wavelength present in the single-phase case is removed from the spectra of $\omega_\theta(r=R_i+d/2, z)$ in the two-phase flow case. A transition from a clear azimuthal wavelength, that characterize the wavy vortices and it is here of wavenumber 4, to a continuous and noisy-dominated spectra, is observed.

Again from this analysis we find that the bubble phase seems to strongly break the coherence of the self-organized vortical structures, as observed in the previous flow visualizations (figure 8). Therefore, differently from the Murai *et al.* (2005) interpretation given for the experiments, we associate the observed two-phase flow drag reduction in the DNS to the breaking and consequent re-arrangement of coherent flow structures rather than to their stretching or displacement. This view will be further supported by the discussion in the next subsection.

3.4. *Explanation for TRR decrease at increasing Re*

We now address the second of our questions, namely, why the drag reduction becomes smaller when increasing the inner cylinder rotational speed. Therefore we look at the global energy balance relation for the torque in the two-phase flow (see the Appendix),

$$T_b = \frac{\pi\rho\left(R_o^2 - R_i^2\right)L}{\Omega}(\langle\varepsilon_b\rangle - \langle \boldsymbol{f}_b \cdot \boldsymbol{u}\rangle) \tag{3.3}$$

$$= \frac{T}{\langle\varepsilon\rangle}(\langle\varepsilon_b\rangle - \langle \boldsymbol{f}_b \cdot \boldsymbol{u}\rangle). \tag{3.4}$$

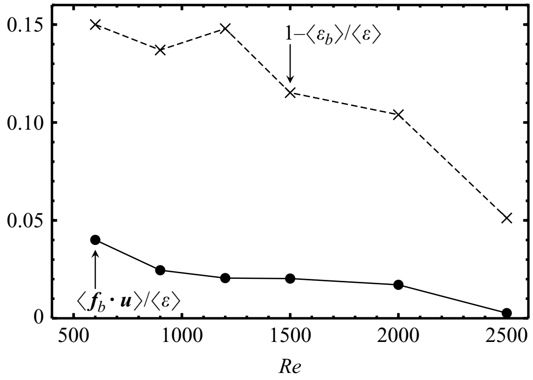

FIGURE 9. The correlation coefficient $\langle \boldsymbol{f}_b\cdot\boldsymbol{u}\rangle/\langle\varepsilon\rangle$ and the relative variation of the mean energy dissipation rate of the two-phase flow compared to the single-phase, $1-\langle\varepsilon_b\rangle/\langle\varepsilon\rangle$, as a function of Re. The sum of the two terms is the total torque reduction ratio (TRR).

The second equation (3.4) follows from relation (2.4). $\mathrm{TRR}=1-T/T_b$ is thus composed of the sum of the two terms

$$\mathrm{TRR}=\left(1-\frac{\langle\varepsilon_b\rangle}{\langle\varepsilon\rangle}\right)+\frac{\langle \boldsymbol{f}_b\cdot\boldsymbol{u}\rangle}{\langle\varepsilon\rangle}, \tag{3.5}$$

which are both of importance here. While the former is associated with changes of the dissipative structures in the system, the latter is associated with the extra energy input in the system due to the bubble momentum transfer. Both these terms are positive (i.e. contribute to the drag reduction). Furthermore, the $1-\langle\varepsilon_b\rangle/\langle\varepsilon\rangle$ term is dominant at all Re, see figure 9. This means that the bubbly phase, which breaks vortical dissipation regions, modifies the energy flux directed from the large scale of the external forcing (due to the rotating cylinder) to the dissipative scale.

Both contributions $1-\langle\varepsilon_b\rangle/\langle\varepsilon\rangle$ and $\langle \boldsymbol{f}_b\cdot\boldsymbol{u}\rangle/\langle\varepsilon\rangle$ to TRR are vanishing at increasing Re. How to explain this dependence? We note that $\langle \boldsymbol{f}_b\cdot\boldsymbol{u}\rangle$, the correlation term of bubble forcing with velocity fluctuations, can be positive for two different reasons. First, the bubbles might distribute preferentially in regions where the velocity is upflow compared to the mean (and for clarity we note that the global mean velocity in the TC system is zero). This would produce a positive correlation with the term $-\boldsymbol{g}$ that is the dominant one in the bubble feedback $\boldsymbol{f}_b$. The second possibility is that bubbles may induce a local upflow fluctuation in the surrounding fluid that is larger than the underlying flow fluctuation. This would always produce a positive correlation with the gravity term $-\boldsymbol{g}$. The latter mechanism, where the bubble perturbation is dominant, is similar to what happens in a system where bubbles are rising in an otherwise quiescent fluid. Therefore, we will call this type of dynamics *pseudo-turbulent*.

In other words, given the assumption $\langle \boldsymbol{f}_b\cdot\boldsymbol{u}\rangle\simeq-\boldsymbol{g}\cdot\langle\boldsymbol{u}\rangle_b$, where $\langle\ldots\rangle_b$ denotes the average on the bubble centroids, we would like to understand the behaviour of $\langle\boldsymbol{u}\rangle_b$ in the different two-phase flow regimes. To distinguish between the two above-mentioned possibilities, we make a numerical test by switching off the two-way coupling, i.e. $\boldsymbol{f}_b=0$. Also in this one-way coupling case bubbles distribute inhomogeneously. In particular, we expect that the bubble distribution in the two-way and one-way coupling cases shares similar properties if the amplitude of fluid fluctuations compared to the bubble feedback is strong enough, while we expect them to have different properties if the pseudo-turbulence mechanism holds. The evaluation

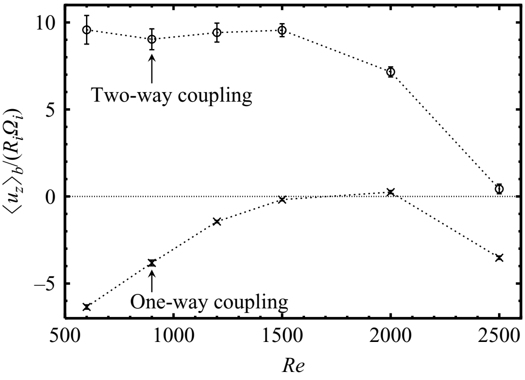

FIGURE 10. Mean vertical fluid velocity at the bubble positions, in dimensionless units $\langle u_z \rangle_b/(\Omega R_i)$ in a one-way and two-way run at variable Re. Bubbles stay preferentially in downflow regions in the former case while in upflow regions for the latter.

of the quantity $\langle u_z \rangle_b$, in particular as a function of Re, allows us to discriminate between the two cases. In figure 10 we show its behaviour both in the one-way and two-way coupling cases. In the one-way coupling case we observe preferential bubble accumulation in downflow regions. More precisely at low Re, from flow and bubble visualization, we may observe that bubbles, while rising, accumulate in stable regions in the flow. The phenomenology of the large-Re regime is rather different: since the flow is time-dependent we do not observe bubble accumulation in stable positions but a rather homogeneous distribution that slightly favours downflow regions. If we consider the two-way coupled case we see that bubbles strongly modify the flow by producing an upward flow at the position where they are. Therefore this test supports the hypothesis of a pseudo-turbulent mechanism acting in the two-phase flow. The pseudo-turbulent mechanism must become less effective at large Re because of the increased level of fluid fluctuations. This is confirmed by measuring the intensity of the vertical anisotropic energy content in the system, figure 11. Vertical anisotropy in the two-phase flow, namely $A_z \equiv \langle u_z'^2 \rangle / \langle u_\theta'^2 + u_r'^2 \rangle$ with $\boldsymbol{u}' = \langle (\boldsymbol{u} - \overline{\boldsymbol{u}}(r))^2 \rangle^{1/2}$ the mean velocity fluctuation, when normalized by the anisotropy in the single-phase case, A_z^{SP}, monotonically decreases for increasing the Reynolds number.

To summarize, the mainly vertical extra forcing exerted by the bubbles on the fluid is responsible for local and anisotropic modifications of the fluid fluctuations. No large-scale flow mechanism induced by bubbles seems to be present or relevant in this process. For increased external forcing (larger Re), the efficiency of the bubbles in perturbing the flow is lost.

3.5. *Bubble distribution*

Inhomogeneous bubble distribution in the TC system is due to the concurrence of several competing factors: (i) the centrifugal force, whose intensity towards the inner wall is proportional to $-u_\theta^2/r$; (ii) inertia that pushes the bubbles towards the local vortical flow structures (Wang & Maxey 1993); (iii) the drift towards the walls, which is a lift effect due to the presence of a local mean shear (Serizawa, Kataoka & Michiyoshi 1975); and finally, (iv) the pseudo-turbulence flow fluctuations which may produce a weak side-by-side bubble–bubble attraction (Zenit, Koch & Sangani 2001; Bunner & Tryggvason 2002). All these effects are included explicitly, or via the bubble–flow interactions, in the numerical model system.

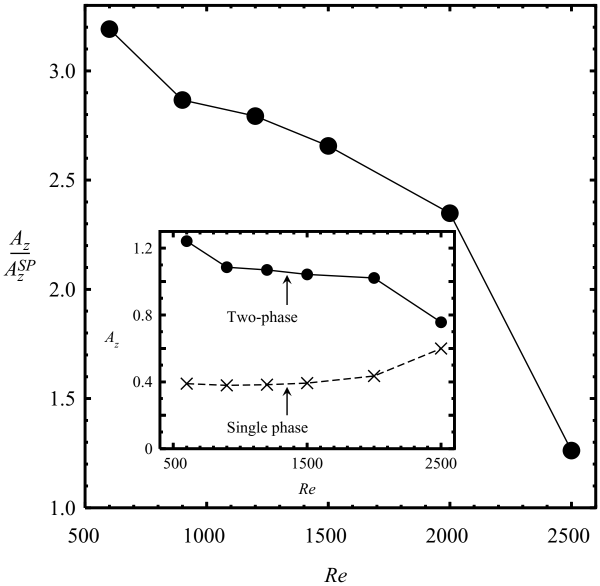

FIGURE 11. The ratio A_z/A_z^{SP} versus Re, with $A_z = \langle u_z'^2 \rangle / \langle u_\theta'^2 + u_r'^2 \rangle$ and $\boldsymbol{u}' = \langle (\boldsymbol{u} - \overline{\boldsymbol{u}}(r))^2 \rangle^{1/2}$ mean velocity fluctuation, evaluated for the two-phase flow A_z^{SP} represents the same quantity evaluated in the single-phase case. In the inset, both A_z and A_z^{SP} are shown separately as a function of Re.

For simplicity we limit our investigation to the radial dependence of mean bubble concentration profiles. The formation of vertical columnar or spiralling structures, similar to the ones experimentally investigated by Shiomi *et al.* (1993), is indeed observed in our numerics, but this will not be the focus of this section. From numerical results reported in figure 5 we have observed that at low Re bubble accumulation at both walls is observed, while at large Re a weak tendency of accumulation in the core is noticeable. Since at the low-Re condition the drag behaviour is dominated by pseudo-turbulence, we attribute near-wall accumulation to the bubble–wall interaction due to the lift in our numerical simulations. More explicitly, the local vertical mean flow produced by the bubble coupling is constrained by the no-slip conditions at the walls. This local upflow profile, as in an upflow vertical pipe (Serizawa *et al.* 1975), induces a lateral (lift-driven) migration to the walls. This is evident if we switch off the lift force. Without lift all the bubbles collapse onto the inner cylinder due to the centripetal force, see figure 12. At large Re the pseudo-turbulent effect is less efficient and the bubbles tend to accumulate in vortex core regions: inertia plays the dominant role. Figure 12 also shows a comparison at $Re = 600$ with the bubble concentration profile measured in the experiment. As noted previously, in the experimental profiles the local void fraction is always peaked near the inner cylinder, in contrast to what is found in the simulations.

What is the main reason for this discrepancy? First, there is the difference in statistical stationarity of the bubbly phase distribution. In the numerics the bubbles are injected statistically homogeneously into the fluid domain and a relatively long time, typically $O(100)$ revolution times, is required until statistical stationarity for the bubbles distribution is reached. In particular, after the bubbles are released in the flow, we observe a transient behaviour in their distribution. Bubbles first accumulate

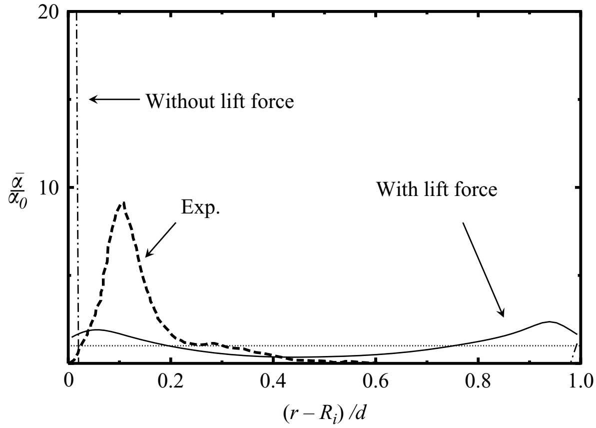

FIGURE 12. Normalized radial mean void fraction at $Re = 600$: a comparison of the numerical results with and without lift force, together with the experimental profiles reported in Murai *et al.* (2005). In the case without lift, nearly all the bubbles collapse into the first compartment of the histogram, giving a sharp bubble concentration whose peak has been truncated for better readability.

in separate columnar regions and then, when flow structures are further broken, they merge into larger domains.

Next, as we have already noted in the introduction, different bubble injection procedures are employed in the numerics and the experiment. In the latter, injection sites are localized at the bottom and near to the inner cylinder wall. From that position bubbles spread to the upper section of the TC flow, where the bubble distributions are finally evaluated. So, it could be that under the particular conditions of slow rotation of the inner cylinder (low Re) stationarity is not fully achieved in the experimental set-up, since the bubbles rise almost vertically. This seems to be supported by some experimental snapshots in Murai *et al.* (2005), see figure 8 of that paper and the corresponding discussion. Furthermore, bubble–bubble coalescence may sporadically occur in the experiment. Coalesced bubbles, which rise faster than the others, lead to the formation of clusters and may delay or prevent the bubble distributions becoming statistically stationary (Y. Murai 2007, personal communication).

Second, on the numerical side, a possible source for the observed discrepancy may lie in the incompleteness of the model adopted for the lift force that may overestimate its relevance. It has been shown (Magnaudet & Legendre 1998) that for non-deformable bubbles, whose Reynolds number (Re_b) is larger than one, and in a pure shear flow the lift coefficient can be considerably smaller than the asymptotic value, $C_L = 1/2$. Similar findings for the lift coefficient have experimentally been obtained by van Nierop *et al.* (2007). Moreover, C_L depends on the local shear and the local vorticity (see also the discussion in Climent, Simonnet & Magnaudet 2007). In order to understand how robust the shape of the mean bubble concentration profile is when changing the lift coefficient C_L, we have performed a test at the lowest Reynolds number ($Re = 600$), where the effect of bubble accumulation on the wall is more intense. C_L has been varied in the interval $[0, 0.5]$ for a set of numerical runs all starting from the same initial condition and continuing until statistically stationarity in time is reached. As shown in figure 13, the bubble mean concentration is rather sensitive to C_L. For the cases with $C_L \leqslant 0.1$ it exhibits a single wall peak near the inner wall. This also implies a dependence on the bubble feedback on the fluid. As reported

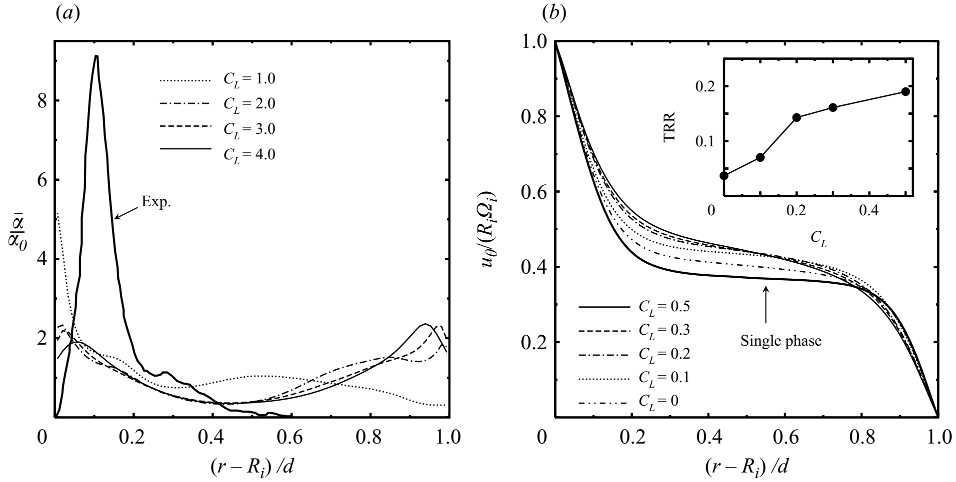

FIGURE 13. Effect of the intensity of the lift force on the bubble mean radial distribution and on the drag reduction. The lift coefficient C_L is varied in the interval $[0, 0.5]$. (*a*) $\overline{\alpha}(r)/\alpha_0$ at changing C_L; (*b*) the corresponding shape of the mean azimuthal velocity profile, $\overline{u_\theta}(r)$. The inset reports the corresponding value of TRR versus C_L.

in figure 13(*b*) (inset), reducing the lift coefficient progressively from $C_L = 0.5$ to zero corresponds to a reduction in TRR. In particular, the accumulation of a small volume concentration of bubbles (here $\alpha_0 = 0.125\,\%$) on the surface of the inner cylinder, as for the cases $C_L = 0$ and $C_L = 0.1$, would have almost no effect on the torque (or drag) modulation and clearly cannot produce the observed axial vortex elongation.

Finally, we note that the point-like coupling adopted in our simulations can only capture the exact flow field, and accurate flow–bubble interactions, far from the bubble sources. Furthermore, bubbles in the simulations may overlap. This could produce overestimates of the bubble feedback, leading to approximate results when looking at the flow and at bubble distributions in highly populated regions.

4. Conclusions

We have numerically investigated the effect of microbubbles on a Taylor–Couette (TC) flow in the wavy vortex flow regime and focused on a comparison with a specific experiment where variations in the drag have been observed. We have demonstrated that this phenomenon is reproduced by an Eulerian–Lagrangian model with point-force coupling. The main effect of microbubbles is to create a local perturbation of the flow, mainly directed upwards in the vertical direction that is able to break the coherent, and mainly dissipative, vortical structures of the flow. This pseudo-turbulent mechanism is at the origin of the torque reduction in the TC flow regime considered here. As a consequence at large Reynolds number (*Re*), where the typical fluid velocity fluctuations are larger and coherent structures are unsteady and less persistent, this mechanism loses its efficiency. The lift force was found to be particularly important in this process. The strength of the lift force is the main factor determining the bubble mean concentration profiles. Furthermore, the drag reduction is particularly sensitive to it. When suppressing the lift, almost no drag reduction is obtained.

The dynamics responsible for the drag reduction in the low-*Re* TC flow highlighted in this study is fundamentally different from that observed in previous highly turbulent experimental investigations by van den Berg *et al.* (2005, 2007). From our numerics it can be extrapolated that small non-deformable bubbles (zero Weber number, *We*), whose size is always below the smallest typical scale of the flow, will be of less and less importance for drag reduction as the external forcing (and hence *Re*) is increased. This is also consistent with the theory developed by L'vov *et al.* (2005), where for small bubbles in a channel flow the expected variation of the drag is only of the order of the void fraction. This suggests that at larger *Re*, when $We > 1$ (as in van den Berg *et al.* 2005, 2007), other physical mechanisms may be effective, namely bubble deformation (Lu *et al.* 2005) or compression (Lo *et al.* 2006) or splitting (Meng & Uhlman 1998). Further joint numerical and experimental works are still needed to clarify this aspect.

We acknowledge Dr Y. Murai for giving us some essential information concerning his experimental setup and measurements and for reading the manuscript.

Appendix

In this Appendix we present a derivation of equations (3.2) and (3.3), based on the use of the reciprocal theorem (Happel & Brenner 1973). Let us introduce two incompressible velocity fields $\boldsymbol{u}$ and $\tilde{\boldsymbol{u}}$, both satisfying the same set of boundary conditions. We identify $\boldsymbol{u}$ as the real flow in the TC system, and $\tilde{\boldsymbol{u}}$ as a particular flow field, that will be specified afterwards. We focus here on the axially periodic TC system with only the inner cylinder rotating. Therefore, the wall boundary conditions are the following:

$$\left.\begin{aligned} \boldsymbol{u} = \tilde{\boldsymbol{u}} = R_i \Omega \boldsymbol{e}_\theta \quad &\text{at} \quad r = R_i, \\ \boldsymbol{u} = \tilde{\boldsymbol{u}} = 0 \quad &\text{at} \quad r = R_o. \end{aligned}\right\} \tag{A 1}$$

The instantaneous, i.e. time-dependent, torque $\mathscr{T}$ acting on the inner cylinder is given by

$$\mathscr{T}\Omega = R_i \Omega \oint_{r=R_i} \mathrm{d}^2\boldsymbol{x}\ (-\boldsymbol{e}_r \cdot \boldsymbol{\sigma} \cdot \boldsymbol{e}_\theta), \tag{A 2}$$

where $\boldsymbol{\sigma}$ is the stress tensor associated with $\boldsymbol{u}$, and $\boldsymbol{e}_r$ and $\boldsymbol{e}_\theta$ are unit vectors in the radial and azimuthal directions, respectively. Using the boundary conditions (A 1) for $\tilde{\boldsymbol{u}}$, we can rewrite (A 2) in a volume integral form

$$\mathscr{T}\Omega = \oint_S \mathrm{d}^2\boldsymbol{x}\ \boldsymbol{n} \cdot \boldsymbol{\sigma} \cdot \tilde{\boldsymbol{u}} = \int_V \mathrm{d}^3\boldsymbol{x}\ (\nabla \cdot \boldsymbol{\sigma}) \cdot \tilde{\boldsymbol{u}} + \int_V \mathrm{d}^3\boldsymbol{x}\ \boldsymbol{\sigma} : \nabla \tilde{\boldsymbol{u}}. \tag{A 3}$$

Here S is the area of the boundaries, V is the fluid volume bounded by S, and the colon represents a product of two dyadics (see e.g. Happel & Brenner 1973, Sec. 2–1). Substituting the momentum equation

$$\nabla \cdot \boldsymbol{\sigma} = \rho(\partial_t \boldsymbol{u} + (\boldsymbol{u} \cdot \nabla)\boldsymbol{u} - \boldsymbol{f}_b)$$

into (A 3), we obtain

$$\mathscr{T}\Omega = \rho \int_V \mathrm{d}^3\boldsymbol{x}[(\partial_t \boldsymbol{u}) \cdot \tilde{\boldsymbol{u}} - (\boldsymbol{u}\boldsymbol{u}) : \tilde{\boldsymbol{S}} - \boldsymbol{f}_b \cdot \tilde{\boldsymbol{u}}] + \rho \oint_S \mathrm{d}^2\boldsymbol{x}\ \underbrace{(\boldsymbol{n} \cdot \boldsymbol{u})}_{=0}(\boldsymbol{u} \cdot \tilde{\boldsymbol{u}}) + \int_V \mathrm{d}^3\boldsymbol{x}\ \boldsymbol{\sigma} : \nabla \tilde{\boldsymbol{u}}, \tag{A 4}$$

where $\boldsymbol{S}(= \{\nabla \boldsymbol{u} + (\nabla \boldsymbol{u})^T\}/2)$ denotes a strain tensor. Similarly to the derivation of (A 3), one can obtain the inner torque $\tilde{\mathscr{T}}$ in the field $(\tilde{\boldsymbol{u}}, \tilde{\boldsymbol{\sigma}})$

$$\tilde{\mathscr{T}}\Omega = \int_V \mathrm{d}^3\boldsymbol{x}\ (\nabla \cdot \tilde{\boldsymbol{\sigma}}) \cdot \boldsymbol{u} + \int_V \mathrm{d}^3\boldsymbol{x}\ \tilde{\boldsymbol{\sigma}} : \nabla \boldsymbol{u}. \tag{A 5}$$

We now apply the Lorentz reciprocal theorem $\boldsymbol{\sigma}:\nabla\tilde{\boldsymbol{u}} = \tilde{\boldsymbol{\sigma}}:\nabla\boldsymbol{u}$ (see e.g. Happel & Brenner 1973, Sec. 3–5) to (A 4) and (A 5), and rewrite the difference of the two torques in the volume integral form,

$$(\mathscr{T}-\tilde{\mathscr{T}})\varOmega = \rho\int_V \mathrm{d}^3\boldsymbol{x}[(\partial_t\boldsymbol{u})\cdot\tilde{\boldsymbol{u}} - (\boldsymbol{u}\boldsymbol{u}):\tilde{\boldsymbol{S}} - \boldsymbol{f}_b\cdot\tilde{\boldsymbol{u}}] - \int_V \mathrm{d}^3\boldsymbol{x}\ (\nabla\cdot\tilde{\boldsymbol{\sigma}})\cdot\boldsymbol{u}. \tag{A 6}$$

From equations (A 4) and (A 6) the relevant relations (3.2) and (3.3) can readily be obtained by proper assumptions on the field $\tilde{\boldsymbol{u}}$. We consider two cases: (i) $\tilde{\boldsymbol{u}}$ is the real flow field $\boldsymbol{u}$, (ii) $\tilde{\boldsymbol{u}}$ is the steady flow field solution of the Stokes equation for the TC system.

Case (i): If we choose the field $(\tilde{\boldsymbol{u}},\tilde{\boldsymbol{\sigma}})$ to be $(\boldsymbol{u},\boldsymbol{\sigma})$, the product $(\boldsymbol{\sigma}:\nabla\tilde{\boldsymbol{u}})$ is equal to the energy dissipation rate $\varepsilon(=2\nu\boldsymbol{S}:\boldsymbol{S})$ and (A 4) becomes

$$\mathscr{T}\varOmega = \frac{\mathrm{d}}{\mathrm{d}t}\int_V \mathrm{d}^3\boldsymbol{x}\ \frac{\rho\boldsymbol{u}\cdot\boldsymbol{u}}{2} + \oint_S \mathrm{d}^2\boldsymbol{x}\ \underbrace{(\boldsymbol{n}\cdot\boldsymbol{u})}_{=0}\frac{\rho\boldsymbol{u}\cdot\boldsymbol{u}}{2} + \rho\int_V \mathrm{d}^3\boldsymbol{x}\ (\varepsilon - \boldsymbol{f}_b\cdot\boldsymbol{u}), \tag{A 7}$$

which corresponds to the kinetic energy transport budget. In a statistically steady state ($\langle \mathrm{d}/\mathrm{d}t\ldots\rangle = 0$), we obtain

$$\frac{T_b\varOmega}{\pi\rho\left(R_o^2-R_i^2\right)L} = \langle\varepsilon\rangle - \langle\boldsymbol{f}_b\cdot\boldsymbol{u}\rangle, \tag{A 8}$$

which accounts for the contribution of the energy dissipation rate and bubble forcing to the time-averaged torque $T_b = \langle\mathscr{T}\rangle$.

Case (ii): We now assume that the field $(\tilde{\boldsymbol{u}},\tilde{\boldsymbol{\sigma}})$ obeys the Stokes equation

$$\nabla\cdot\tilde{\boldsymbol{\sigma}} = 0. \tag{A 9}$$

Imposing the boundary conditions (A 1), we write the solution of circular Couette flow (see Chandrasekhar 1961, Chapter VII)

$$\tilde{\boldsymbol{u}} = \boldsymbol{e}_\theta\left(\frac{-R_i r + R_o^2 R_i r^{-1}}{R_o^2 - R_i^2}\right)(R_i\varOmega),\quad \tilde{\boldsymbol{S}} = -(\boldsymbol{e}_r\boldsymbol{e}_\theta + \boldsymbol{e}_\theta\boldsymbol{e}_r)\frac{R_o^2 R_i r^{-2}}{R_o^2 - R_i^2}(R_i\varOmega). \tag{A 10}$$

Substituting (A 9) and (A 10) into (A 6), and assuming a statistical state, we determine the mean torque

$$T_b = T_l\left(1 + \frac{Re\left(R_o^2 - R_i^2\right)\eta}{2(R_i\varOmega)^2(1-\eta)}\left\langle\frac{u_r u_\theta}{r^2} - \frac{\left(R_o^2 - r^2\right)f_{b,\theta}}{2R_o^2 r}\right\rangle\right), \tag{A 11}$$

where T_l denotes the torque in the laminar flow,

$$T_l = \frac{4\pi\rho(R_i\varOmega)^2R_i^2L}{Re\ \eta(1+\eta)}. \tag{A 12}$$

The first term inside the angle brackets on the right-hand side of (A 11) accounts for the laminar flow contribution and the second term for the modification from the circular Couette flow due to the nonlinearity of the fluid motion and the bubble forcing. Using the area-averaged quantities $\overline{u_r u_\theta}(r)$ and $\overline{f_{b,\theta}}(r)$, we may finally write (A 11) in the radial integral form, used in the main paper,

$$T_b = T_l\left(1 + \frac{Re\ \eta}{(R_i\varOmega)^2(1-\eta)}\int_{R_i}^{R_o}\mathrm{d}r\ \left(\frac{\overline{u_r u_\theta}(r)}{r} - \frac{\left(R_o^2 - r^2\right)\overline{f_{b,\theta}}(r)}{2R_o^2}\right)\right). \tag{A 13}$$

We note that a general identity providing the effect of the Reynolds shear stress distribution on the skin friction has been recently derived by Fukagata, Iwamoto & Kasagi (2002) for the case of a pressure-driven channel and circular pipe flows. The Fukagata *et al.* identity has been further extended to the problem of channel flow with mixed boundary conditions by using the reciprocal theorem in Sbragaglia & Sugiyama (2007). Our derivation presented above represents an extension of that work to the TC system.

REFERENCES

Andereck, C. D., Liu, S. S. & Swinney, H. L. 1986 Flow regimes in a circular Couette system with independently rotating cylinders. *J. Fluid Mech.* **164**, 155–183.

Auton, T. R. 1987 The lift force on a spherical body in a rotational flow. *J. Fluid Mech.* **183**, 199–218.

Auton, T. R., Hunt, J. C. R. & Prud'homme, M. 1988 The force exerted on a body in inviscid unsteady non-uniform rotational flow. *J. Fluid Mech.* **197**, 241–257.

van den Berg, T. H., van Gils, D. P. M., Lathrop, D. P. & Lohse, D. 2007 Bubbly turbulent drag reduction is a boundary layer effect. *Phys. Rev. Lett.* **98**, 084501.

van den Berg, T. H., Luther, S., Lathrop, D. P. & Lohse, D. 2005 Drag reduction in bubbly Taylor–Couette turbulence. *Phys. Rev. Lett.* **94**, 044501.

van den Berg, T. H., Luther, S. & Lohse, D. 2006 Energy spectra in microbubbly turbulence. *Phys. Fluids* **18**, 038103.

Bunner, B. & Tryggvason, G. 2002 Dynamics of homogeneous bubbly flows Part 1. Rise velocity and microstructure of the bubbles. *J. Fluid Mech.* **466**, 17–52.

Calzavarini, E., van den Berg, T., Toschi, F. & Lohse, D. 2008 Quantifying microbubble clustering in turbulent flow from sigle-point measurements. *Phys. Fluids* **20**, 040702.

Chandrasekhar, S. 1961 *Hydrodynamic and Hydromagnetic Stability*. Clarendon.

Climent, E. & Magnaudet, J. 1999 Large-scale simulations of bubble-induced convection in a liquid layer. *Phys. Rev. Lett.* **82**, 4827–4830.

Climent, E., Simonnet, M. & Magnaudet, J. 2007 Preferential accumulation of bubbles in Couette-Taylor flow patterns. *Phys. Fluids* **19**, 083301.

Djeridi, H., Gabillet, C. & Billard, J. Y. 2004 Two-phase Couette–Taylor flow: Arrangement of the dispersed phase and effects on the flow structures. *Phys. Fluids* **16**, 128–139.

Dominguez-Lerma, M. A., Ahlers, G. & Cannell, D. 1984 Marginal stability curve and linear growth rate for rotating Couette–Taylor flow and Rayleigh–Bénard convection. *Phys. Fluids* **27**, 856–860.

Dutcher, C. S. & Muller, S. J. 2007 Explicit analytic formulas for Newtonian Taylor–Couette primary instabilities. *Phys. Rev.* E **75**, 047301.

Eckhardt, B., Grossmann, S. & Lohse, D. 2000 Scaling of global momentum transport in Taylor–Couette and pipe flow. *Eur. Phys. J.* B **18**, 541–544.

Eckhardt, B., Grossmann, S. & Lohse, D. 2007 Torque scaling in turbulent Taylor–Couette flow between independently rotating cylinders. *J. Fluid Mech* **581**, 221–250.

Esser, A. & Grossmann, S. 1996 Analytic expression for Taylor–Couette stability boundary. *Phys. Fluids* **8**, 1814–1819.

Ferrante, A. & Elghobashi, S. 2004 On the physical mechanisms of drag reduction in a spatially-developing turbulent boundary layer laden with microbubbles. *J. Fluid Mech.* **503**, 345–355.

Fukagata, K., Iwamoto, K. & Kasagi, N. 2002 Contribution of Reynolds stress distribution to the skin friction in wall-bounded flows. *Phys. Fluids* **14**, L73–L76.

Fukagata, K. & Kasagi, N. 2002 Highly energy-conservative finite difference method for the cylindrical coordinate system. *J. Comput. Phys.* **181**, 478–498.

Grace, J. 1973 Shapes and velocities of bubbles rising in infinite liquids. *Trans. Inst. Chem. Engrs* **51**, 116–120.

Happel, J. & Brenner, H. 1973 *Low Reynolds Number Hydrodynamics*, 2nd Edn. Martinus Nijhoff.

Hunt, J. C. R., Wray, A. A. & Moin, P. 1988 Eddies, stream and convergence zones in turbulent flows. *Report* CTR-S88. Center for Turbulence Research, NASA Ames Research Center and Stanford University, California, USA.

Lathrop, D. P., Fineberg, J. & Swinney, H. L. 1992 Transition to shear-driven turbulence in Couette–Taylor flow. *Phys. Rev.* A **46**, 6390–6405.

Lim, T. T. & Tan, K. S. 2004 A note on power-law scaling in a Taylor–Couette flow. *Phys. Fluids* **16**, 140–144.

Lo, T. S., L'vov, V. S. & Procaccia, I. 2006 Drag reduction by compressible bubbles. *Phys. Rev.* E **73**, 036308.

Lu, J., Fernández, A. & Tryggvason, G. 2005 The effect of bubbles on the wall drag in a turbulent channel flow. *Phys. Fluids* **17**, 095102.

L'vov, V. S., Pomyalov, A., Procaccia, I. & Tiberkevich, V. 2005 Drag reduction by microbubbles in turbulent flows: The limit of minute bubbles. *Phys. Rev. Lett.* **94**, 174502.

Madavan, N. K., Deutsch, S. & Merkle, C. L. 1984 Reduction of turbulent skin friction by microbubbles. *Phys. Fluids* **27**, 356–363.

Magnaudet, J. & Legendre, D. 1998 Some aspects of the lift force on a spherical bubble. *Appl. Sci. Res.* **58**, 441–461.

Maxey, M. R. & Riley, J. J. 1983 Equation of motion for a small rigid sphere in a nonuniform flow. *Phys. Fluids* **26**, 883–889.

Mazzitelli, I. M., Lohse, D. & Toschi, F. 2003*a* On the relevance of the lift force in bubbly turbulence. *J. Fluid Mech.* **488**, 283–313.

Mazzitelli, I. M., Lohse, D. & Toschi, F. 2003*b* The effect of microbubbles on developed turbulence. *Phys. Fluids* **15**, L5–L8.

Meng, J. C. S. & Uhlman, J. S. 1998 Microbubble formation and splitting in a turbulent boundary layer for turbulence reduction. *Proc. Intl Symp. on Seawater Drag Reduction, Newport, RI, July, US Office of Naval Research, Arlington, VA*, pp. 341–355.

Murai, Y., Oiwa, H. & Takeda, Y. 2005 Bubble behavior in a vertical Taylor–Couette flow. *J. Phys. Conf. Ser.* **14**, 143–156.

van Nierop, E. A., Luther, S., Bluemink, J. J., Magnaudet, J., Prosperetti, A. & Lohse, D. 2007 Drag and lift forces on bubbles in a rotating flow. *J. Fluid Mech.* **571**, 439–454.

Oiwa, H. 2005 A study of mechanisms modifying shear stress in bubbly flow. Doctoral Thesis, Fukui University, Japan.

Sanders, W. C., Winkel, E. S., Dowling, D. R., Perlin, M. & Ceccio, S. L. 2006 Bubble friction drag reduction in a high-Reynolds-number flat-plate turbulent boundary layer. *J. Fluid Mech.* **552**, 353–380.

Sbragaglia, M. & Sugiyama, K. 2007 Boundary induced nonlinearities at small Reynolds numbers. *Physica* D **228**, 140–147.

Serizawa, A., Kataoka, I. & Michiyoshi, I. 1975 Turbulence structure of air-water bubbly flow – II. Local properties. *Intl J. Multiphase Flow* **2**, 235–246.

Shiomi, Y., Kutsuma, H., Akagawa, K. & Ozawa, M. 1993 Two-phase flow in an annulus with a rotating inner cylinder (flow pattern in bubbly flow region). *Nucl. Engng Des.* **141**, 27–34.

Tanahashi, M., Iwase, S. & Miyauchi, T. 2001 Appearance and alignment with strain rate of coherent fine scale eddies in turbulent mixing layer. *J. Turb.* **2**, 1–17.

Taylor, G. I. 1923 Stability of a viscous liquid contained between two rotating cylinders. *Phil. Trans. R. Soc. Lond.* A **223**, 289–343.

Wang, L. P. & Maxey, M. R. 1993 The motion of microbubbles in a forced isotropic and homogeneous turbulence. *Appl. Sci. Res.* **51**, 291–296.

Wendt, F. 1933 Turbulente Strömungen zwischen zwei rotierenden konaxialen Zylindern. *Ing.-Arch.* **4**, 577–595.

Xu, J., Maxey, M. R. & Karniadakis, G. E. M. 2002 Numerical simulation of turbulent drag reduction using micro-bubbles. *J. Fluid Mech.* **468**, 271–281.

Zenit, R., Koch, D. L. & Sangani, A. S. 2001 Measurements of the average properties of a suspension of bubbles rising in a vertical channel. *J. Fluid Mech.* **429**, 307–342.